

Assessment of oil spills using Sentinel 1 C-band SAR and Landsat 8 multispectral sensors

Niyazi Arslan 

Received: 13 June 2018 / Accepted: 28 September 2018 / Published online: 18 October 2018
© Springer Nature Switzerland AG 2018

Abstract Environmental pollution and disasters have gradually increased with the growth of the population. Surveillance of the effects of these incidents is very important for public health. Satellite missions are a very efficient tool for identifying pollutants such as oil spills. The synthetic aperture radar (SAR) sensor is an active microwave sensing system that can be used for oil spill applications with optical sensors mounted on Landsat 8, Sentinel 2, and Advanced Spaceborne Thermal Emission and Reflection Radiometer (ASTER) satellite systems taking into account cloud coverage and revisiting time of the satellite at the same location. In this study, the oil spill area caused by a ship running aground at 13:40 local time (LT) on 18 December 2016 was studied on the coast of Ildir Bay (Izmir, Turkey) with Sentinel 1 SAR and Landsat 8 multispectral sensors. Different image-processing techniques were applied to Landsat 8 bands such as minimum noise fraction (MNF), morphology, and convolution filters in order to highlight the oil spill area related to the incident. In the detection stage, oil slicks and look-alikes were successfully distinguished by analyzing the SAR data with Landsat 8 results and the location of the ship. With the visual interpretation of the results, the selected techniques are consistent with each other in terms of showing oil spill areas.

Keywords Oil spill · Synthetic aperture radar · Landsat 8 · Image processing

Introduction

Oil spills have adverse effects on the marine environment in oceanic and coastal areas. Coastal areas are places with high population density. In the case of oil spills in coastal areas, the spread of oil should be monitored before and after this event in order to ensure that the shoreline is safe from pollutants. Oil spills can occur from oil pipeline cracks, illegal discharge from ships, ship incidents, and from oil drilling platforms. In coastal areas, oil spills mostly occur due to illegal discharge and ship incidents.

Various techniques have been developed to monitor oil spills such as visual surveys with aircraft, microwave radiometers (MWR), infrared line scanner (IR), laser fluoro sensor (LFS), side-looking airborne radar (SLAR), synthetic aperture radar (SAR), and optical sensors (such as Landsat, Sentinel 2, Advanced Spaceborne Thermal Emission and Reflection Radiometer (ASTER)) (Gade et al. 1998, 2013; Richards 1999; Shuchman et al. 2004; Montali et al. 2006; Solberg et al. 2007; Trivero et al. 2007; Gade 2015; Misra and Balaji 2017). From these techniques, remote sensing satellite sensors working with different bandwidths in the electromagnetic spectrum, such as visible, near infrared, shortwave infrared, thermal infrared (optical sensors), and radar (SAR), can be used more efficiently because

N. Arslan (✉)
Department of Geomatics Engineering, Cukurova University,
Ceyhan Campus, 01950, Ceyhan, Adana, Turkey
e-mail: niyazi.arslan@gmail.com

of continuous monitoring and wide global coverage of the Earth. SAR satellites provide data in all weather conditions including day and night. Oil spill monitoring with SAR theoretically depends on the dampening of the capillary waves in different wind speed conditions resulting in dark formations. Wind speed is a very important parameter for this dark formation. If the wind speed is lower than 2 m/s, the sea surface does not give any sign of the oil spill on SAR images. In order to define oil spill, the wind speed should be between 3 and 6 m/s. Moreover, thick oil spills can be defined with wind speeds between 10 and 12 m/s. As a result, the wind speed should range between 2.5 and 12 m/s in order to detect oil spills with SAR observations (Lawal et al. 2016).

There are several system-dependent parameters (configuration) that affect the processing of SAR data for oil spill monitoring. The first parameter is radar bands. Remote sensing satellites equipped with SAR sensors send a signal at different frequencies labeled as X-band (8–12 GHz, 2.5–4 cm), C-band (4–8 GHz, 4–8 cm), and L-band (1–2 GHz, 15–30 cm). X-band is more sensitive to sea surface waves due to its short wavelength providing higher contrast between oil and oil-free sea surface. But it includes a high amount of speckle noise (Garcia-Pineda et al. 2017). Marzialetti and Laneve (2016) stated that the contrast between the oil spill and sea surface is high in X-band, medium in C-band, and low in L-band. X-band gives better results than C-band radar and L-band radar. However, C-band and even L-band SAR data give good information about oil spills (Marzialetti and Laneve 2016; Fingas and Brown 2017, 2018). The second parameter is the polarization type of the SAR system. Because of the high dielectric constant of the sea surface, VV polarization gives much more radar backscatter compared with HH polarization. VV polarization radar gives a better signal-to-noise ratio resulting in more contrast in the oil spill area as well. So, VV polarization can be used more efficiently in oil spill studies (Alpers and Espedal 2004; Alpers and Melsheimer 2004).

The main problem for oil spill studies with SAR images is to separate the oil spill and look-alikes as they produce similar characteristic dark spots. Look-alikes can occur from biogenic films, low wind speed, internal waves, ship wakes, grease ice, algae, shallow water, and rain cells. For this reason, a multisensor approach can be applied to the areas with oil spills in order to support the discrimination of oil spill from look-alikes. In addition

to SAR, optical sensors can be used to validate SAR results for oil spills. The response of optical sensors to oil spill also changes with respect to light conditions, film thickness, and optical properties of oil and sea. Optical sensors are also affected by high cloud coverage and fog that should be considered when processing optical images. Operational remote sensing optical sensors, such as Sentinel 2, Landsat 8, and ASTER, play an efficient role in oil spill monitoring. Integration of different optical sensors is inevitable to obtain reliable oil spill results as the sensing capabilities are dependent on effects such as the position of the pollution, the different geometry of acquisition, the progress of oil spill, sensor specification, revisiting time of the satellites, spatial coverage, and cloud coverage. As each sensor mounted on the carrying platform has special characteristics in the design stage, a combination of the information from all sensors presents more reliable results in modeling the extent and spread of oil spills (Zhao et al. 2014).

There are several studies related with SAR and optical sensors. Majidi et al. (2018b) studied Sentinel 1 C-band dual polarization (VV/VH) data from the Persian Gulf. They reported that VV polarization gives better results than the VH polarization. Zhao et al. (2014) carried out an oil spill study in a shallow coastal sea in the Arabian Gulf using Moderate Resolution Imaging Spectroradiometer (MODIS), Medium Resolution Imaging Spectrometer Instrument (MERIS), and Landsat 7 ETM+ and Landsat 8 data for three different events. They concluded that the oil spill areas have dark or bright features because of the variations in oil type, thickness of oil, solar, and viewing geometry. Xing et al. (2015) examined the accidental oil spill from the Deep-water Horizon in the Gulf Mexico on April 20, 2010. They used daytime images of Landsat 7 ETM+ and Landsat 5 TM thermal bands that show oil spill areas with a temperature 0.6 K lower than the oil-free sea surface. Majidi et al. (2018a) investigated an oil spill in shallow water in the Al Khafji field in the Persian Gulf that occurred on July 2017 with Sentinel 2 images.

Image processing of the raw data is also important to highlight areas affected by oil spills. These methods can be applied to the studies related with optical and SAR sensors. In Kolokoussis and Karathanassi (2018), object-based image analysis (OBIA) was applied to Sentinel 2 in order to detect oil spill near the shore. This analysis depends on the segmentation of the image using homogeneity and geometric criteria resulting in objects. Fana et al. (2015) studied support vector

machines for oil spill monitoring using SAR images. Sun et al. (2013) used Robert operator, Sobel operator, Laplacian operator and LOG operator to define the oil spill edge in the Penglai 19-3 oil accident using MODIS remote sensing data. Dool et al. (2014) applied Sobel and Prewitt edge detectors to highlight remarkable edges in the SAR images. In addition, morphological dilation filter is implemented on SAR data in order to make features more noticeable.

In this study, Sentinel 1 data was analyzed to detect an oil spill while Landsat 8 data was used for validation purposes. Brightness temperatures were estimated from Landsat 8 thermal band 10 in order to observe oil spill changes in temperature on the sea surface. Minimum noise fraction, morphology dilation, and Sobel edge detection filters were applied to Landsat 8 bands for determination of the oil spill region.

Study area and data

General description of the study area

While a cargo ship in motion was maneuvering to avoid hitting a fishing boat, it ran aground on rocks near Fener (Ufak) Island, Cesme, Turkey (Fig. 1). The sea vessel incident occurred on 18 December 2016. The size of the ship was 121-m length and 17-m width. It led to the greatest environmental disaster in the history of Cesme.

Oil leaked into the sea due to a gash in the body of the ship. When the situation was reported, the crew arriving in the region set up a barrier to prevent leakage of the oil on board. However, the rescue of the ship and environmental cleanup work could not be started due to the weather conditions.

After the storm, the leaking oil from the ship was quickly controlled. When cleaning work involving a 100-person cleaning crew was carried out, 30 t of the 50-t oil slick were cleaned. The city of Cesme was saved at the brink of a much greater catastrophe. Even though the barriers around the ship controlled the oil spill, they were breached during a second storm on 22 December causing new pollution spreading 50 t of fuel oil. Starting at 10:00 a.m. on 27 December, the ship was removed from the rocks as a result of 12 h of work. Then, the ship was towed to a safe region between the south of Fener Island and the west of Celebi Island, and it was anchored here to allow an investigation. In summary, a commercial ship ran aground on a rocky place and fuel oil

leaking into the sea spread over a large area. The main motivation here is to develop a method based on SAR and Landsat 8 data so that the location of the oil slick can be monitored with high accuracy (UBAK 2018).

SAR and Landsat 8 data

In this study, Sentinel 1 SAR and Landsat 8 multispectral remote sensing satellite data was used. The Sentinel 1 is a C-band SAR instrument with a central frequency of 5.405 GHz corresponding to a wavelength of ~ 5.55 cm operated in single polarization (HH or VV) and dual polarization (HH + HV or VV + VH). Sentinel 1A and Sentinel 1B satellites are in the same orbit to help increase the imaging frequency as the temporal resolution is reported to be 6 days (SUHET 2013; Bourbigot et al. 2016; ESA 2018). The SAR data used is given in Table 1 which was acquired at ground range detected (GRD) processing level and in the interferometric wide swath (IW) mode. The dual-polarized Sentinel 1 SAR data for the study area on the relevant dates were downloaded from the Copernicus Open Access Hub of the European Space Agency. Four days of SAR data are represented by the specification (14, 19, 20, and 26 December 2016). Level 1 IW GRD product is multilooked and projected to ground range using an Earth ellipsoid model. Ground range coordinates are the slant range coordinates projected onto the ellipsoid of the Earth. In this product, pixels are converted to almost square spatial resolution and square pixel spacing by using multilooking with reduced speckle noise at the cost of lower resolution for the pixels (ESA 2018).

In order to strengthen the results from SAR analysis, Landsat 8 bands can also be used to determine oil spills (Table 1). There are only one set of data available from Landsat 8 after the ship incident as most of the data has high cloud coverage (20 December 2016). The Landsat 8 image covers the area of 185 km \times 180 km with 16-day repeat cycle. The data is stored in L1T format in 16-bit digital numbers (DN). The L1T products are given in the Universal Transverse Mercator (UTM) map projection with World Geodetic System 84 (WGS84) datum. This data is radiometrically calibrated and orthorectified using ground control points and digital elevation model (DEM) (Roy et al. 2014).

For Landsat 8 data, 11 bands were used for processing which can be seen in Table 2. The cloud coverage is 2% for the selected data. The bands from 1 to 9 are Operational Land Imager (OLI), and bands 10 and 11

Fig. 1 Location map of the study area

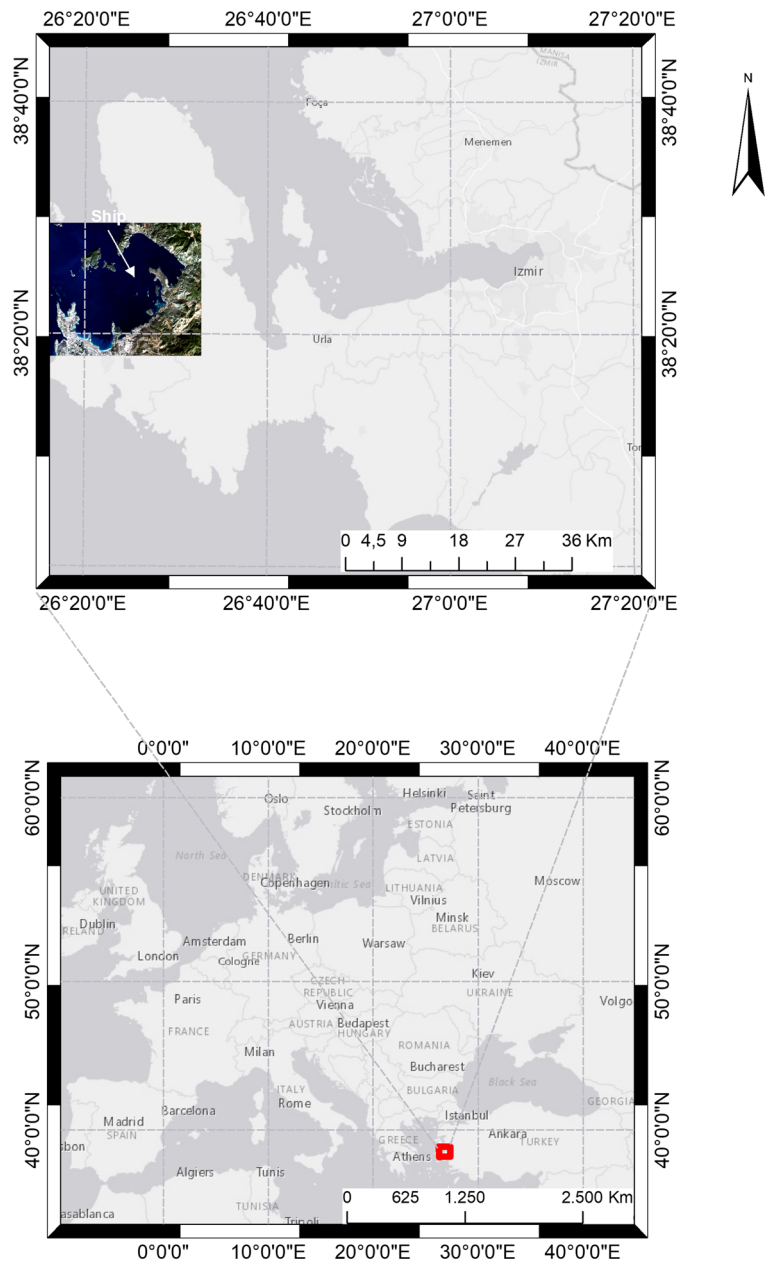


Table 1 The list of used data

Satellite system	Date	Time	Product type	Incidence angles	Acquisition orbits	Mode	Dual polarization
Sentinel 1A	14 December 2016	16:06:48	GRD	30.52–46.42	Ascending	IW	VV + VH
Sentinel 1B	19 December 2016	04:22:20	GRD	30.56–45.99	Descending	IW	VV + VH
Sentinel 1A	20 December 2016	04:14:51	GRD	30.65–46.16	Descending	IW	VV + VH
Sentinel 1B	26 December 2016	04:14:08	GRD	30.60–46.05	Descending	IW	VV + VH
Landsat 8	20 December 2016	08:52:36	OLI-TIRS	–	–	–	–

Table 2 The list of used bands for Landsat 8

Bands	Wavelength (μm)	Resolution (m)
Band 1—Ultra Blue (coastal/aerosol)	0.435–0.451	30
Band 2—Blue	0.452–0.512	30
Band 3—Green	0.533–0.590	30
Band 4—Red	0.636–0.673	30
Band 5—Near Infrared (NIR)	0.851–0.879	30
Band 6—Shortwave Infrared (SWIR) 1	1.566–1.651	30
Band 7—Shortwave Infrared (SWIR) 2	2.107–2.294	30
Band 8—Panchromatic	0.503–0.676	15
Band 9—Cirrus	1.363–1.384	30
Band 10—Thermal Infrared (TIRS) 1	10.60–11.19	100 (30)
Band 11—Thermal Infrared (TIRS) 2	11.50–12.51	100 (30)

are Thermal Infrared Sensor (TIRS) (Barsi et al. 2014). TIRS bands are resampled to 30 m from 100-m spatial resolution in order to make connections between bands for mathematical computations in Landsat operation center. In Landsat 8 products, spatial resolution for thermal bands is delivered at 30 m. In this study, the map projection was UTM Zone 35/WGS 1984.

Methodology

Sentinel 1A and 1B data were used for oil spill monitoring. Different polarization schemes can be used for monitoring oil spills. The dampening effect is the principle underlying the oil spill detection methodology in SAR (Topouzelis et al. 2007; Topouzelis et al. 2009). When the radar signal is sent to the sea, oil slicks can be detected because of the dampening effect of oil on capillary waves. Radar images have an advantage for oil spill detection as the oil can be detected as black patches on images. In addition to SAR images, Landsat 8 bands can be used by applying different filters. Brightness temperature is used in oil spill analysis as well.

The work flow sequence of the processing for monitoring possible oil spills on the sea using Sentinel 1 and Landsat 8 data is shown in Fig. 2.

SAR data processing

Sentinel Application Platform (SNAP) software is jointly developed by Brockmann Consult and is used to process Sentinel 1 Level 1 IW GRD images for generation of geocoded, calibrated (slope normalized), multilooked,

despeckled sigma0_VV product for VV polarization. The preprocessing steps of the SAR data are given in Fig. 2 (Minchella 2016). In the first step of the processing, Sentinel 1 precise orbit files that are available some time from the production of SAR data are applied because of the low accuracy of the orbit state vector supplied in the metadata. Later, thermal noise removal is carried out. Thermal noise decreases the accuracy of radar reflectivity estimates due to the background energy in the SAR system. In the next step, calibration of the VV polarization digital pixels is carried out by using parameters (system dependent) given in the SAR product file for radiometrically calibrated backscatter values (sigma 0). SAR images also include speckle noise that can be seen in the image as a salt-and-pepper effect. Multilooking is a method that reduced the inherent speckled appearance by using two approaches. Multilooked images can be generated in the frequency domain using subspectral bandwidth or space-domain averaging of a single look image, either with or without specific 2D kernels by convolution. SNAP uses the space domain approach to resample images to a lower resolution (mean GR square pixel as 20 m) to decrease speckle noise level using multilooking for azimuth (1) and range (1). While Sentinel 1 GRD products are multilooked, speckle noise reduction can be carried out using different filters taking into account the distribution of the data. In order to reduce the speckle noise, speckle filtering option is used by selecting a 5 × 5 window size gamma map filter in SNAP. Two studies can be given that suggest gamma map filter. Meenakshi and Punitham (2011) studied the mean, median, Lee sigma, local-region, Lee, gamma MAP for speckle noise reduction on SAR images. The gamma map filter has the property of

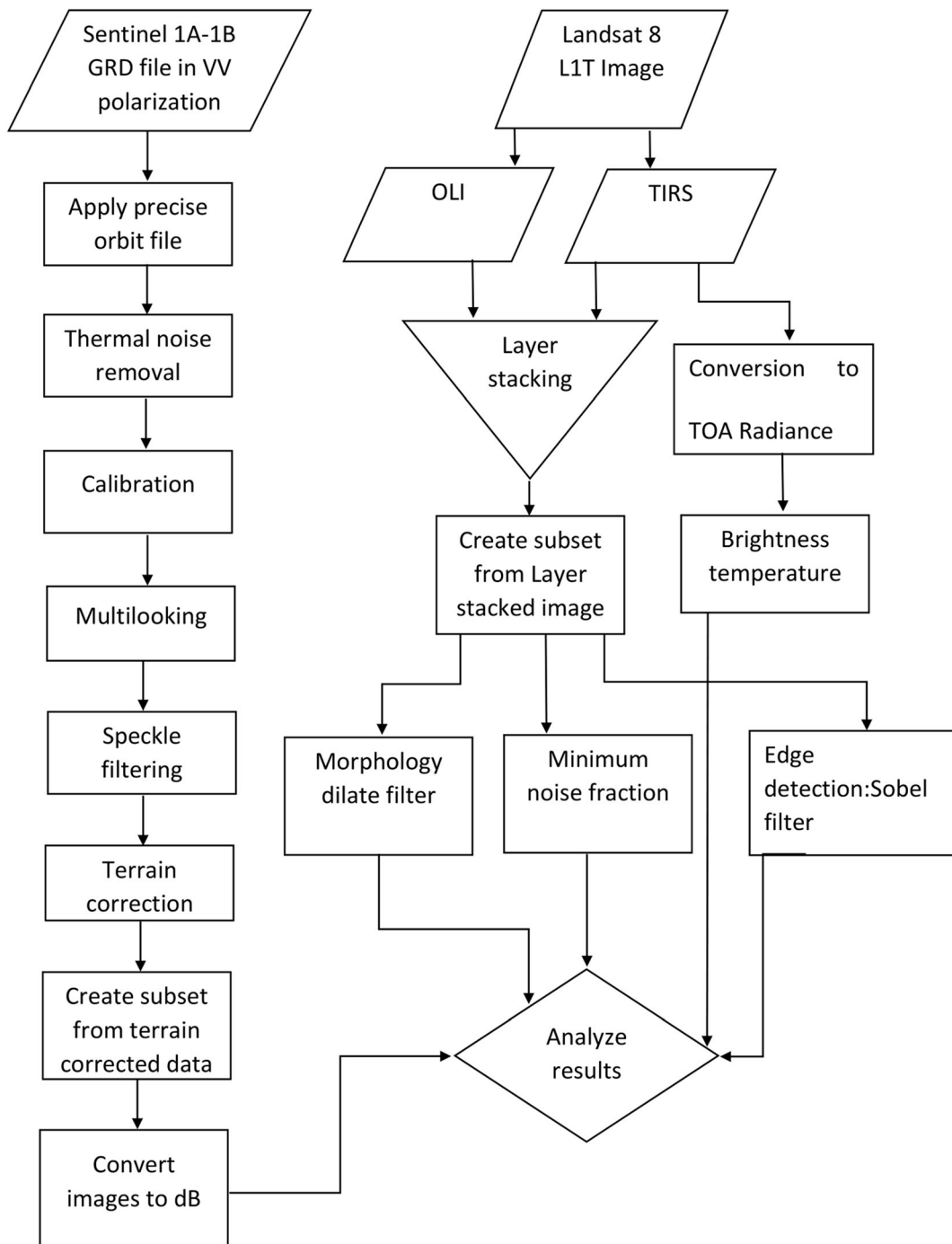


Fig. 2 Work flow used in the study

preserving edge information compared with other methods. In addition, they stated that the gamma map, Frost, and Lee filters with a 5×5 kernel show better results for SAR images. Sudha and Vijendran (2017) used six filter techniques with five different kernel sizes for

reducing speckle noise on Sentinel 1 data, and they found that 7×7 window size gamma map filter provided better results than the other methods. After the speckle filtering, the terrain correction is applied to output data using Range Doppler Terrain Correction Operator in SNAP because

the distance between the SAR sensor and the reflected surface can be distorted due to the tilt of the sensor and topographic changes. The images should be corrected for these effects in the terrain correction step by using digital elevation model (DEM). SRTM (3 s) is used for DEM. Moreover, the source GR Pixel spacing is obtained from the multilooking step as 20 m in the range and azimuth directions (square pixel) that represents distance on the ground for a pixel. The pixel spacing for the resulting product is selected as 20 m representing ground distance. WGS 84 datum was chosen for map coordinate system in terrain correction resulting in a geocoded image. The subset of the area of interest is cropped from the terrain-corrected image and converted to dB.

Landsat 8 data processing

Landsat 8 Level 1 (L1T) data is given in DN. In order to estimate brightness temperature from Landsat 8 thermal bands, the conversion was made from DN using the constants in the metadata file. There are two steps in the algorithm for estimation of brightness temperature, one of which is conversion to top of atmosphere (TOA) radiance and the other is conversion to TOA brightness temperature.

Conversion to top of atmosphere radiance

TOA spectral radiance can be estimated from Landsat Level 1 data in DN with Eq. 1 as follows:

$$L_\lambda = M_L Q_{cal} + A_L \tag{1}$$

In this equation, L_λ is the TOA spectral radiance ($W/(m^2 \text{ srad } \mu m)$), $M_L = 0.00033420$ is the band-specific multiplicative rescaling factor, $A_L = 0.10000$ is the band-specific additive rescaling factor, and Q_{cal} is the quantified and calibrated standard product (L1T) pixel values (DN).

Conversion to top of atmosphere brightness temperature

TOA spectral radiance from the first step can be converted to TOA brightness temperature using Eq. 2:

$$T = \frac{K_2}{\ln\left(\frac{K_1}{L_\lambda + 1}\right)} \tag{2}$$

In this equation, T is the TOA brightness temperature (Kelvin) and $K_1 = 774.8853$ and $K_2 = 1321.0789$ are the

band-specific thermal conversion constants. It should be noted that the parameters K_1 , K_2 , M_L , and A_L are obtained from the metadata file for the related data (USGS 2018).

Minimum noise fraction

The mathematical concept of the MNF is dependent on the principal component analysis (PCA) method. In the MNF method, noise fraction is minimized recursively by using the same eigenvalues and eigenvectors obtained from the PCA resulting in uncorrelated output bands (Green et al. 1988; Berman et al. 2012). Most of the information can be found in the first output bands. Data comprise d dimensions and n pixels. Let \mathbf{X} show the size of $n \times d$ data matrix with the size of $d \times 1$ vector of \mathbf{X}_i , $i = 1, 2, 3, \dots, n$:

$$\mathbf{X} = (\mathbf{X}_1, \dots, \mathbf{X}_n)^T \tag{3}$$

\mathbf{X}_i can be obtained from the sum of signal (\mathbf{S}_i) and noise (ϵ_i) as:

$$\mathbf{X}_i = \mathbf{S}_i + \epsilon_i \tag{4}$$

If there is no correlation between signal and noise, the covariance of \mathbf{X}_i can be represented as follows:

$$\sum_{\mathbf{X}}^T = \sum_{\mathbf{X}}^S + \sum_{\mathbf{X}}^N \tag{5}$$

where $\sum_{\mathbf{X}}^T$ is the covariance of \mathbf{X}_i , $\sum_{\mathbf{X}}^S$ is the covariance of \mathbf{S}_i , and $\sum_{\mathbf{X}}^N$ is the covariance of ϵ_i . For mathematical computations, the covariance matrices of the signal and noise are diagonalized by using the Λ matrix with $d \times d$ dimension which includes the eigenvectors of the data (Eq. 6).

$$\Lambda \sum_{\mathbf{X}}^S \Lambda^T = \Lambda \sum_{\mathbf{X}}^N \Lambda^T = \mathbf{I} \tag{6}$$

In this equation, Λ is a diagonal matrix of eigenvalues as $\lambda_1 \geq \lambda_2 \geq \dots \lambda_d \geq 0$ and \mathbf{I} is the identity matrix. In order to solve Eq. 6, the generalized eigendecomposition method can be used for transformations (Green et al. 1988; Berman et al. 2011).

Filters

In this study, two different filters were used: morphology dilation and Sobel edge detection. In the morphology dilation filter, the aim is to fill the holes between pixels suppressing noise resulting in a smooth surface on a gray image. This filter can be referred to as non-linear image-

processing technique focusing on geometric structures within an image. Dilation filters use set theory. Dilation combines two sets (**A** and **B**) using vector addition of set elements. **A** can be mentioned as the image whereas **B** is a structure element, namely, kernel. In this study, kernel size is selected as a 3×3 matrix (**B**) (Haralick et al. 1987).

The aim of the edge detection algorithms is to define discontinuity in the intensity function or very steep gradient in the image. One of the edge detection methods is the convolution Sobel detection filter that can be used to define the gradients in the image. These gradients show the edge of the grayscale image. When the gradient is high in some pixel in the image, the method defines that pixel as an edge (Shrivakshan and Chandrasekar 2012). The Sobel edge detection method uses two 3×3 convolution filters. Each 3×3

convolution filter is separately moved in x and y direction over each pixel of the grayscale image resulting in a gradient component in these two perpendicular directions. Gradient in x -direction can be called G_x , while in y -direction, it is G_y (Vincent and Folorunso 2009; Narendra and Hareesh 2011). Both of them can be combined to find the absolute magnitude of the gradient in each pixel ($|G|$) and the orientation (θ) of that gradient, respectively, with Eqs. 7 and 8 as follows:

$$|G| = \sqrt{G_x^2 + G_y^2} \quad (7)$$

$$\theta = \arctan(G_y/G_x) \quad (8)$$

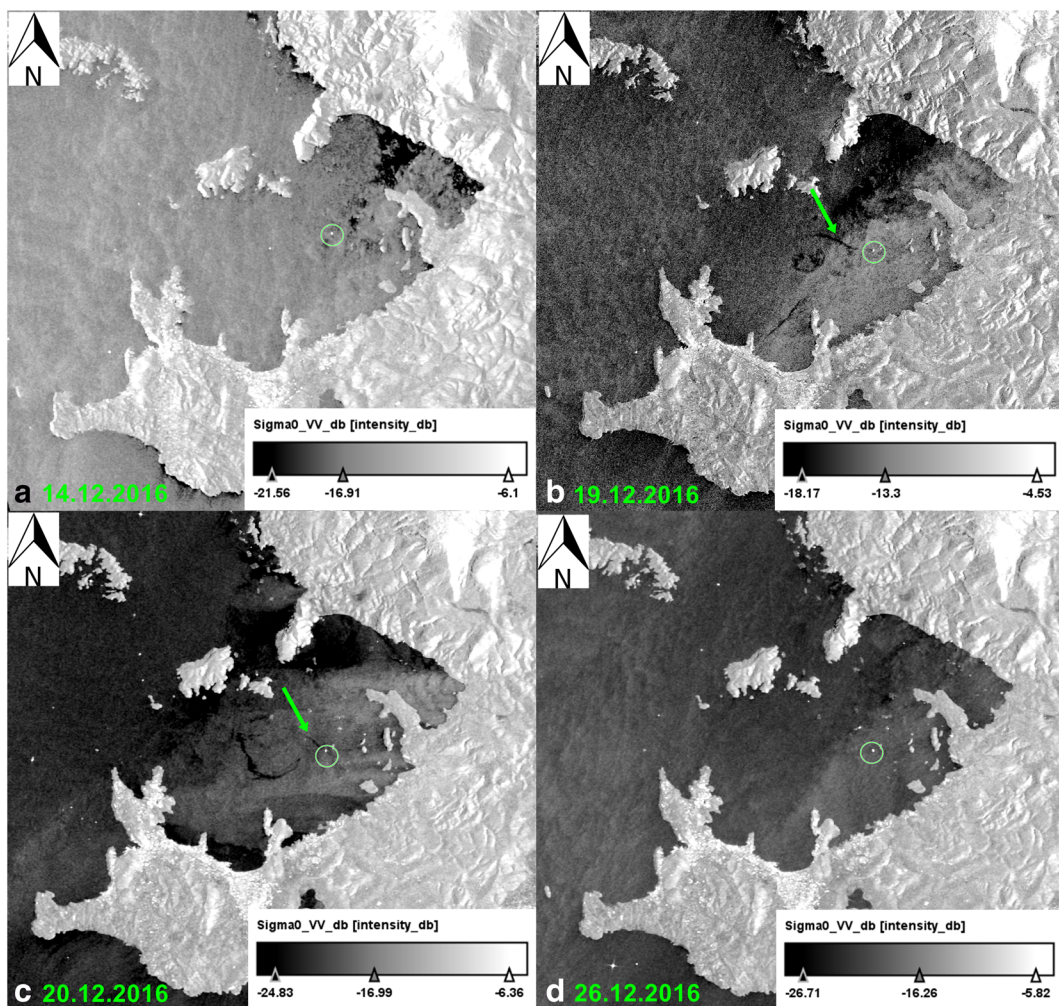


Fig. 3 Oil spill stages: **a** data acquired on 14 December 2016, **b** data acquired on 19 December 2016, **c** data acquired on 20 December 2016, and **d** data acquired on 26 December 2016

3 × 3 convolutional filter in x-direction and y-direction can be given as follows:

$$x_{filter} = \begin{bmatrix} -1 & 0 & 1 \\ -2 & 0 & 2 \\ -1 & 0 & 1 \end{bmatrix} \tag{9}$$

$$y_{filter} = \begin{bmatrix} 1 & 2 & 1 \\ 0 & 0 & 0 \\ -1 & 2 & -1 \end{bmatrix} \tag{10}$$

Results and discussion

In order to detect the oil spill, the downloaded Sentinel 1A-1B images were processed with the given methodology and analyzed in SNAP. The first image was acquired on 14 December 2016 (Fig. 3a). In this image, some different contrast areas were observed for the VV mode. There is no distinct feature related to oil spills. The wind shadow areas that are generally seen near the coastal region were observed in the image while operating in VV mode. Furthermore, these areas may also occur due to biogenic films, wind speed, and internal waves. The site of the ship is depicted by the green

circle. In this figure, the ship is far from the incident region as it loads fish from the fish farm. Afterwards, the ship moved from the departure point but ran aground on rocks under the sea. Figure 3b shows the first image, which was acquired by Sentinel 1B, after the accident. In this figure, there are varieties of look-alikes, but there is a region like an arc near the ship indicated by a green arrow. It may be related to the oil spill event.

The third image is from a time after the ship incident on 20 December 2016. After the ship incident, it was reported that the oil was spilled and leaking onto the sea surface in the shape of an arc (Fig. 3c). In this figure, an arc-shaped area was observed in the VV mode (green arrow). It exactly verifies the reported geographical location of the ship in Ildır Bay (UBAK 2018). The last image is from a time 8 days after the ship incident on 26 December 2016. There are no black contrast areas related with the incident around the ship. The relation between the oil spill area can be seen as similar black patches around the ship on 19 and 20 December 2016. In order to support findings from SAR images, Landsat 8 data was processed by using different image-processing algorithms.

Thermal infrared sensors sense the oil spill areas as well. Thermal infrared bands can be converted to brightness temperatures for easy representation of the

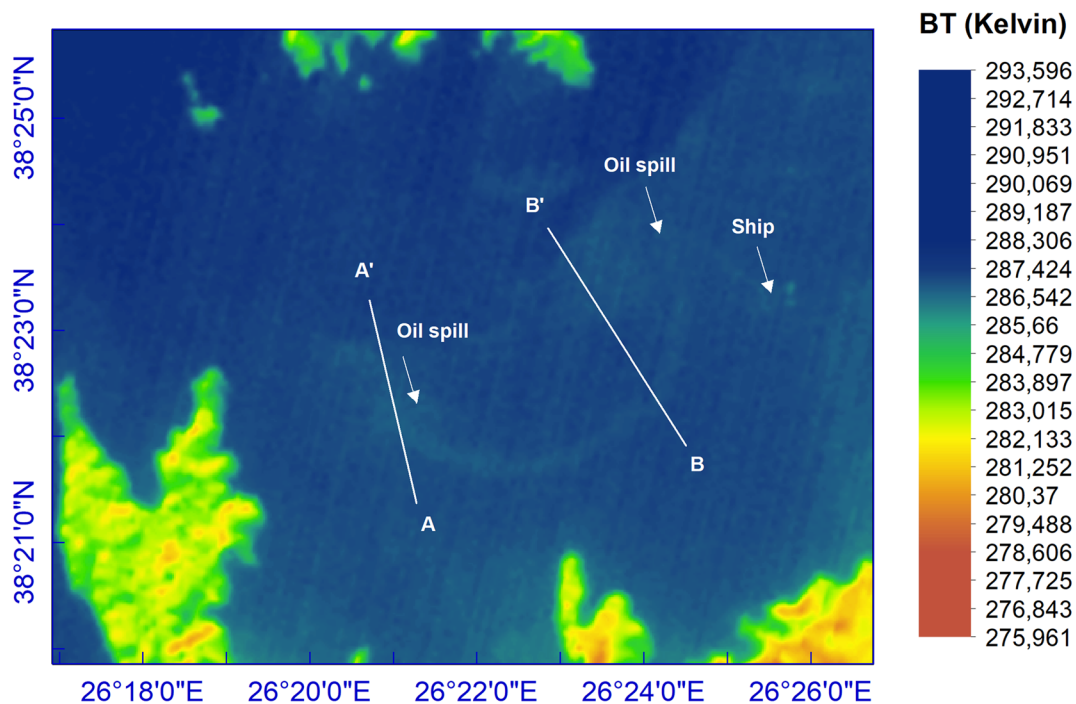


Fig. 4 The brightness temperature values for Landsat 8 thermal band 10 on 20 December 2016

image. The brightness temperatures can be estimated by using the values in metadata for the Landsat TIR band with Planck's equation (USGS 2018). Figure 4 shows brightness temperature values range from 275.961 K to 293.596 K. The position of the ship is shown by the white arrow. The track of the oil spill area can be seen as a line and arc with different contrast than the area outside the affected area (white arrow). The regions detected in SAR image can be seen in the area obtained from thermal image as well.

In order to show the affected area more clearly, two arbitrary profiles AA' and BB' are taken from brightness temperature and are represented in Fig. 5a, b.

Figure 5a, b shows AA' cross section and BB' cross section. In Fig. 5a, minimum brightness temperature value is about 286.5 K coinciding with oil spill areas that are shown as red dashed lines. The maximum values are about 287 and 287.2 K around the oil spill area. In Fig. 5b, minimum values are about 286.64 and 286.80 K whereas maximum values are about 287.1 and

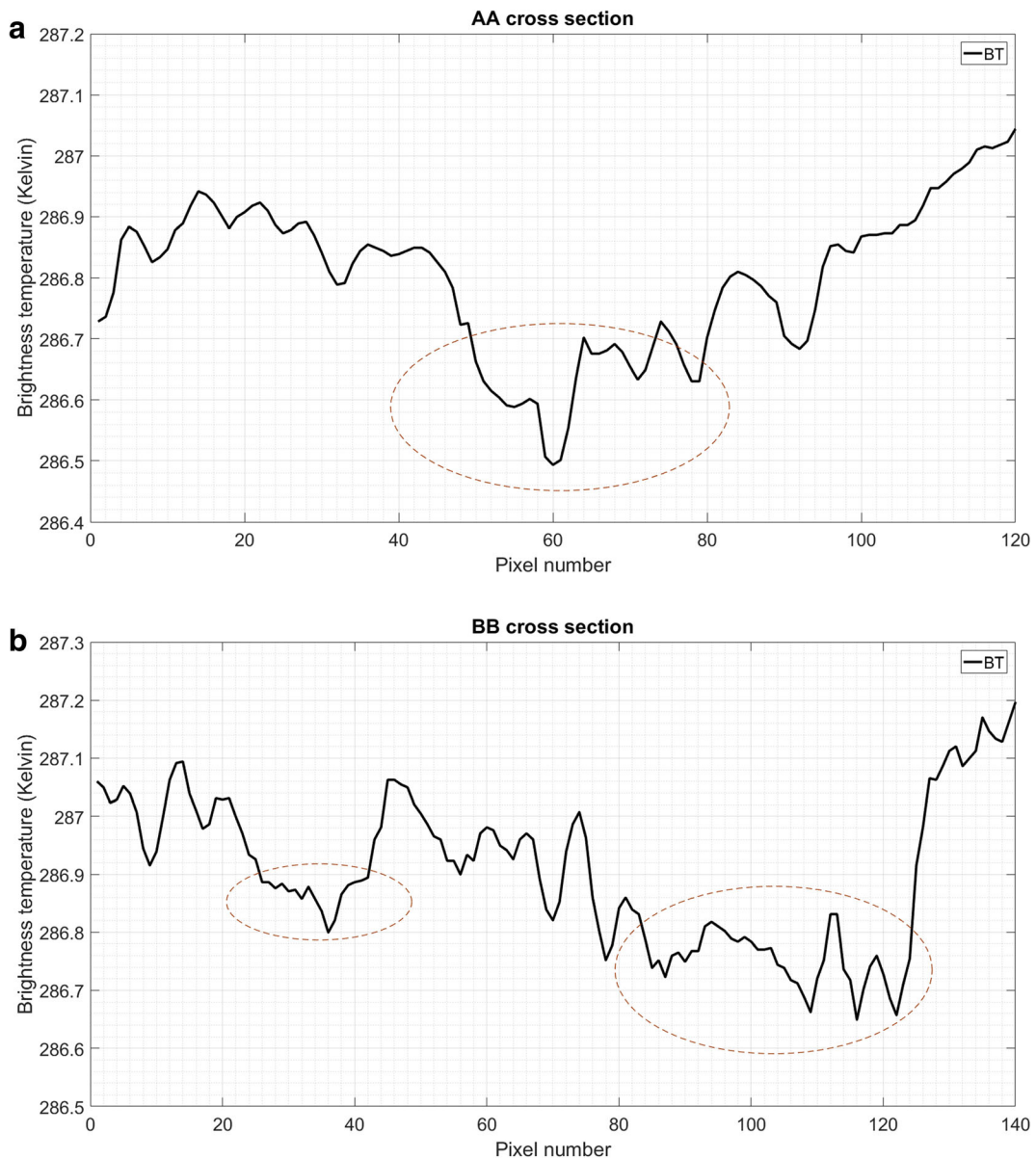


Fig. 5 **a** Cross section of AA' and **b** cross section of BB' from brightness temperature images of Landsat 8 thermal band 10 on 20 December 2016

287.2 K. The minimum values are related with the oil spill area. Salisbury et al. (1993) estimated the emissivity of seawater as 0.989 for Landsat Thematic Mapper (TM) wavelength (10.40–12.50 μm). At this wavelength, aged crude oil slicks have emissivity of 0.96. The change in the emissivity of 0.01 results in 0.6 $^{\circ}\text{C}$ variation in temperature. This situation can be related with the contrast in brightness temperature in Landsat TM band 6 resulting in maximum change of up to 1.74 $^{\circ}\text{C}$ at room temperature (Salisbury et al. 1993). In our study, the changes in brightness temperature are about 0.6 K which corresponds to emissivity value of 0.01. Oil films on the sea surface can be seen in Landsat thermal band 10 as dark contrast with low brightness temperature. Klemas (2010) classified thermal response with respect to thick or thin layers of oil spill. Klemas (2010) mentioned that layers thicker than 150 μm appear hot or bright, whereas layers less than 50 μm thick appear cool and dark.

In the next step, a morphology dilation filter was applied to Landsat 8 bands. Red (R), green (G), and blue (B) (RGB) image is constructed by applying filtered thermal infrared, blue, and coastal/aerosol bands, respectively. After the filtering procedure, the extent of the oil spill area can be seen more easily. Figure 6a depicts RGB image of morphology dilation filter applied to thermal infrared, blue, and coastal/aerosol bands. The white arrow in this figure shows the intense oil spill as silvery areas. The track of the oil spill starts from the back of the ship following the area as shown by the white arrow. The convolutional Sobel filter was also applied to all Landsat bands in order to show the edge of oil spill area. Figure 6b shows the convolutional Sobel filter applied to blue, coastal/aerosol, and green bands in RGB. Sobel filter results show the edge of the affected area caused by the ship incident.

Moreover, the minimum noise fraction (MNF) method was applied to 11 bands of Landsat 8 image in order to show the contribution of all bands for oil spill incidents. This method can be used to distinguish the area with oil spill that has different contrast from surrounding areas. Eleven bands of Landsat 8 image were selected as input resulting in 11 output bands after processing. Figure 7 depicts RGB image of the MNF output bands 8, 7, and 6. In this figure, oil spill areas are shown with white arrows. The coastal areas can be seen as green. In oil spill studies, the most important issue is to separate oil spill areas from look-alikes. For Sentinel 1 SAR images, it is hard to separate look-alikes from the real

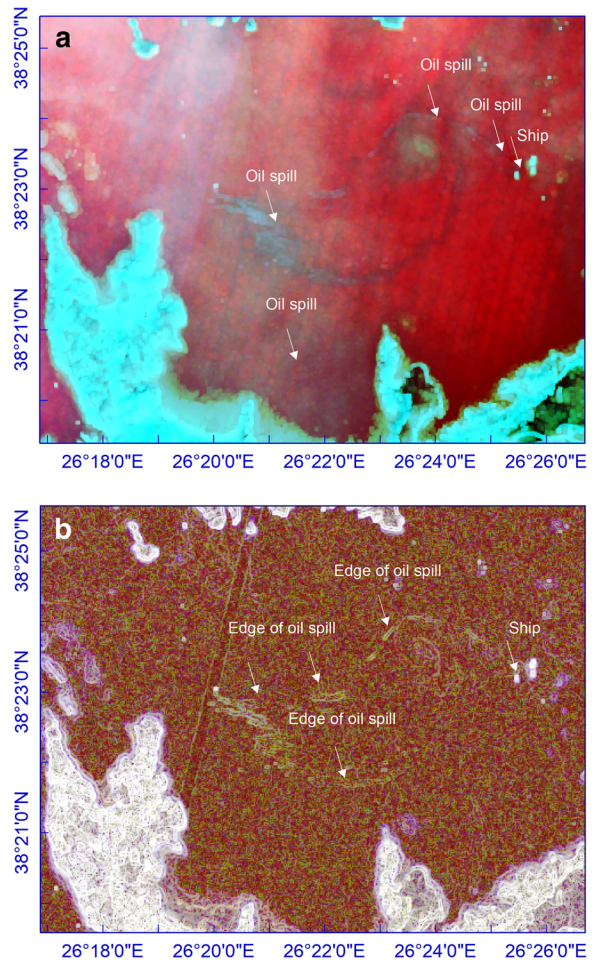
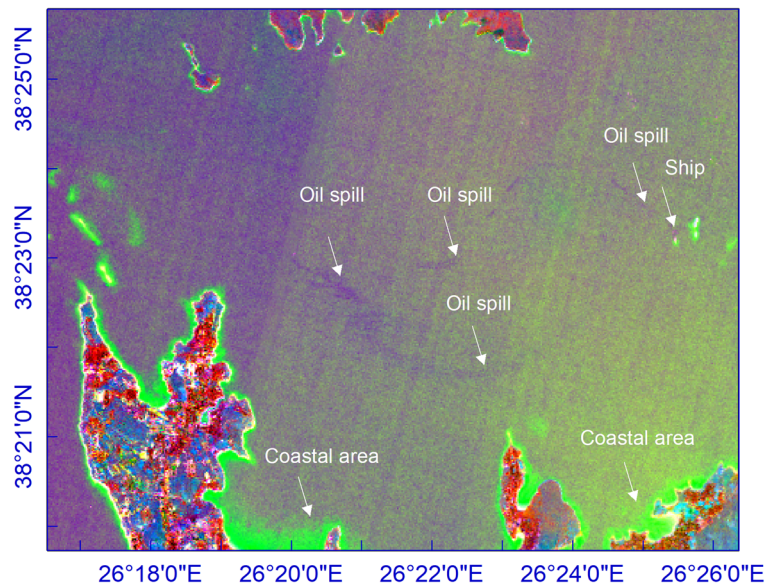


Fig. 6 RGB images of **a** morphology dilation filtered thermal infrared, blue, and coastal/aerosol bands and **b** convolutional Sobel filtered blue, coastal/aerosol, and green bands

oil spill area as the backscattering of the radar signal gives similar dB values as wind effect, algae, and the coastline. Even though the ground truth data supports the findings from SAR data, it is important to use different optical sensors or SAR systems to validate the results. The coverage, data availability, satellite revisit time, and cloud coverage also restrict data processing of oil spills. Moreover, Sentinel 2 and remaining Landsat 8 data could not be used because of high cloud coverage in the selected days. There is no ASTER data for the incident location for related days as well. Different filters are efficiently used to highlight the oil spill area. The coastline can be seen as green color in MNF results (Fig. 7) and can be addressed as a low depth and rocky sea bed. This situation can cause false detection of oil spills. So, this kind of effect can also be considered in oil spill studies. The ship incident report found in

Fig. 7 RGB of MNF bands of 8, 7, and 6, respectively



UBAK (2018) has detailed information about the oil spill event as well. Ground truth data from UBAK (2018) supports our findings.

Conclusions

Satellite-based remote sensing is an effective tool for emergency situations where it is not possible to perform fast and effective on-site measurements. There are different satellite missions to monitor the Earth. Sentinel 1 SAR and Landsat 8 satellite can be used to detect oil spills. Monitoring of the direction and magnitude of spilled oil on the sea surface, especially due to accidents involving marine vessels, is very important in terms of ecosystem and environmental effects. In this study, SAR and Landsat 8 satellite images were used to determine the efficiency of oil spill detection. A major environmental disaster caused by an incident in Ildır Bay was used for detailed analysis. The satellite images for the related dates in the substages of this incident were subjected to a number of procedures. The results showed that the oil spill area can be identified by using Sentinel 1 data using VV polarized images. The study showed that the oil spill and slick after a sea incident can be determined quickly, effectively, and economically with the aid of satellite images. In addition, different scenarios, including weather events and marine waves, should be considered in the analysis in order to use remote sensing as an effective tool for monitoring oil

spills. The methods in this study can be used to make quick decisions about reducing environmental impacts during and after any oil spill event. MNF, morphology, and convolution filters were successfully applied to Landsat 8 data for oil spill determination. The results support the Sentinel 1 processing results.

Acknowledgements The author would like to thank the European Space Agency (ESA) for providing Sentinel 1 data and USGS for Landsat 8 data. Finally, the satellite imagery was processed using SNAP.

Funding information This study was supported by Cukurova University, Scientific Research Projects Coordination Unit (FBA-2017-8601).

References

- Alpers, W., & Espedal, H. A. (2004). Oil and surfactants. In C. R. Jackson & J. R. Apel (Eds.), *Synthetic aperture radar marine User's manual* (pp. 263–275). Washington, DC: National Oceanic and Atmospheric Administration (NOAA).
- Alpers, W., & Melsheimer, C. R. (2004). Rainfall. In C. R. Jackson & J. R. Apel (Eds.), *Synthetic aperture radar marine User's manual* (pp. 355–371). Washington, DC: National Oceanic and Atmospheric Administration (NOAA).
- Barsi, J. A., Lee, K., Kvaran, G., Markham, B. L., & Pedelty, J. A. (2014). The spectral response of the Landsat-8 operational land imager. *Remote Sensing*, 6, 10232–10251.
- Berman, M., Phatak, A., & Traylen, A. (2012). Some invariance properties of the minimum noise fraction transform. *Chemometrics and Intelligent Laboratory Systems*, 117, 189–199.

- Bourbigot, M., Johnsen, H., Piantanida, R., & Hajduch, G. (2016). Sentinel-1 product definition. Technical report, Report number: S1-RS-MDA-52-7440.
- Dool, R. V. D., Kleynhans, W., & Schwegmann, C. P. (2014). Monitoring bilge oil dumping in the ocean using SAR image processing techniques. AARSE 10th international conference 27–31 October, Johannesburg, South Africa.
- ESA (2018). <https://earth.esa.int/web/sentinel/technical-guides/sentinel-1-sar/products-algorithms/level-1-algorithms/ground-range-detected>. Accessed 20 September 2018.
- Fana, J., Zhangb, F., Zhaob, D., & Wang, J. (2015). Oil spill monitoring based on SAR remote sensing imagery. *Aquatic Procedia*, 3, 112–118.
- Fingas, M., & Brown, C. E. (2017). Oil spill remote sensing. In M. Fingas (Ed.), *Oil spill science and technology* (pp. 305–385). Cambridge, MA: Elsevier.
- Fingas, M., & Brown, C. E. (2018). A review of oil spill remote sensing. *Sensors*, 18(91). <https://doi.org/10.3390/s18010091>.
- Gade, M. (2015). Synthetic aperture radar applications in coastal waters. Proceedings of the twelfth international conference on the Mediterranean coastal environment MEDCOAST 06–10 October, Varna, Bulgaria.
- Gade, M., Alpers, W., Huhnerfuss, H., Wisman, V. R., & Lange, P. A. (1998). On the reduction of the radar backscatter by oceanic surface films: scatterometer measurements and their theoretical interpretation. *Remote Sensing of Environment*, 66(1), 52–70.
- Gade, M., Byfield, V., Ermakov, S., Lavrova, O., & Mitnik, L. (2013). Slicks as indicators for marine processes. *Oceanography*, 26(2), 138–149.
- Garcia-Pineda, O., Holmes, J., Rissing, M., Jones, R., Wobus, C., Svejksky, J., & Hess, M. (2017). Deepwater horizon oil spill using synthetic aperture radar (SAR). *Remote Sensing*, 567(9), 1–19.
- Green, A., Berman, M., Switzer, P., & Craig, M. (1988). A transformation for ordering multispectral data in terms of image quality with implications for noise removal. *IEEE Transactions on Geoscience and Remote Sensing*, 26, 65–74.
- Haralick, R. M., Sternberg, S. R., & Zhuang, X. (1987). Image analysis using mathematical morphology. *IEEE Transactions on Pattern Analysis and Machine Intelligence*, 9(4), 532–550.
- Klemas, V. (2010). Tracking oil slicks and predicting their trajectories using remote sensors and models: Case studies of the sea princess and deepwater horizon oil spills. *Journal of Coastal Research*, 26(5), 789–797.
- Kolokoussis, P., & Karathanassi, V. (2018). Oil spill detection and mapping using sentinel 2 imagery. *Journal of Marine Science and Engineering*, 6, 4. <https://doi.org/10.3390/jmse6010004>.
- Lawal, A. D., Radice, G., Ceriotti, M., & Makarfi, A. U. (2016). Investigating SAR algorithm for Spaceborne interferometric oil spill detection. *International Journal of Engineering and Technical Research*, 4(3), 2454–4698.
- Majidi, N. M., Groppi, D., Laneve, G., Marzioletti, P., & Piras, G. (2018a). Oil spill detection analyzing sentinel 2 satellite images: a Persian gulf case study, proceedings of the 3rd world congress on civil, structural, and environmental engineering (CSEE'18) Budapest, Hungary, April 8–10.
- Majidi, N. M., Groppi, D., Marzioletti, P., Piras, G., & Laneve, G. (2018b). Mapping sea water surface in Persian Gulf, oil spill detection using Sentinel-1 images. Proceedings of the 4th World Congress on New Technologies (NewTech'18), Madrid, Spain, August 19–21.
- Marzioletti, P., & Laneve, G. (2016). Oil spill monitoring on water surfaces by radar L, C and X band SAR imagery: a comparison of relevant characteristics. In Proceedings of the 2016 IEEE International Geoscience and Remote Sensing Symposium (IGARSS), Beijing, China, 10–15 July, 7715–7717.
- Meenakshi, A. V., & Punitham, V. (2011). Performance of speckle noise reduction filters on active radar and SAR images. *International Journal of Technology and Engineering System*, 2(1), 111–114.
- Minchella, A. (2016). *ESA SNAP-Sentinel-1 training course*. Harwell: Satellite Applications Catapult - Electron Building.
- Misra, A., & Balaji, R. (2017). Simple approaches to oil spill detection using sentinel application platform (SNAP)-ocean application tools and texture analysis: a comparative study. *Journal of the Indian Society of Remote Sensing*, 45, 1065–1075. <https://doi.org/10.1007/s12524-016-0658>.
- Montali, A., Giacinto, G., Migliaccio, M., & Gambardella, A. (2006). Supervised pattern classification techniques for oil spill classification in SAR images: preliminary results. Proceedings of the SEASAR2006 workshop, ESA-ESRIN, Frascati, Italy.
- Narendra, V. G., & Hareesh, K. S. (2011). Study and comparison of various image edge detection techniques used in quality inspection and evaluation of agricultural and food products by computer vision. *International Journal of Agriculture and Biological Engineering*, 4(2), 1–8.
- Richards, J. A. (1999). *Remote sensing digital image analysis: an introduction*. Berlin: Springer-Verlag.
- Roy, D. P., Wulder, M. A., Loveland, T. R., Woodcock, C. E., Allen, R. G., Anderson, M. C., Helder, D., Irons, J. R., Johnson, D. M., Kennedy, R., Scambos, T. A., Schaaf, C. B., Schott, J. R., Sheng, Y., Vermote, E. F., Belward, A. S., Bindschadler, R., Cohen, W. B., Gao, F., Hipple, J. D., Hostert, P., Huntington, J., Justice, C. O., Kilic, A., Kovalsky, V., Lee, Z. P., Lyburner, L., Masek, J. G., McCorkel, J., Shuai, Y., Trezza, R., Vogelmann, J., Wynne, R. H., & Zhu, Z. (2014). Landsat-8: science and product vision for terrestrial global change research. *Remote Sensing of Environment*, 145, 154–172.
- Salisbury, J. W., D'aria, D. M., & Sabins, F. F. (1993). Thermal infrared remote sensing of crude oil slicks. *Remote Sensing of Environment*, 45, 225–231.
- Shrivakshan, G. T., & Chandrasekar, C. (2012). A comparison of various edge detection techniques used in image processing. *IJCSI International Journal of Computer Science Issues*, 9(5–1), 269–276.
- Shuchman, R., Onstott, R., Johannessen, O., Sandven, S., & Johannessen, J. (2004). Processes at the Ice edge—The Artic. In *Synthetic Aperture Radar marine user's manual*. Cap.18. NOAA.
- Solberg, A., Brekke, C., & Husoy, P. (2007). Oil spill detection in Radarsat and ENVISAT SAR images. *IEEE Transactions on Geoscience and Remote Sensing*, 45(3), 746–755.
- Sudha, V., & Vijendran, A. S. (2017). Evaluation of speckle reduction filtering techniques on SAR images. International Conference On Intelligent Computing and Technology, December, 8, India.

- SUHET (2013). *Sentinel-1 user handbook*. European Space Agency. <https://sentinel.esa.int/web/sentinel/user-guides/sentinel-1-sar>. Accessed 12 June 2018.
- Sun, M. P., Shi, C. Y., & Li, H. Y. (2013). Comparison operator edge detection based on remote sensing of marine oil spill. *Advanced Materials Research*, 610-613, 3747–3751.
- Topouzelis, K., Karathanassi, V., Pavlakis, P., & Rokos, D. (2007). A new object-oriented methodology to detect oil spills using Envisat images. Proceedings of the Envisat Symposium Montreux, Switzerland.
- Topouzelis, K., Stathakis, D., & Karathanassi, V. (2009). Investigation of genetic algorithms contribution to feature selection for oil spill detection. *International Journal of Remote Sensing*, 30, 611–625.
- Trivero, P., Biamino, W., & Nirchio, F. (2007). High resolution COSMO-SkyMed SAR images for oil spills automatic detection. Proceedings of the geoscience and remote sensing symposium, IGARSS 2007 IEEE International: 2–5.
- UBAK. (2018). Ship incident report (in Turkish). http://www.ubak.gov.tr/BLSM_WIYS/KAIK/tr/Deniz_Rapor/20171221_120141_76347_1_76648.pdf. Accessed 12 June 2018.
- USGS. (2018). Using USGS Landsat 8 product. <https://landsat.usgs.gov/using-usgs-landsat-8-product>. Accessed 12 September 2018.
- Vincent, O. R., & Folorunso, O. (2009). A descriptive algorithm for Sobel image edge detection. Proceedings of Informing Science & IT Education Conference.
- Xing, Q., Li, L., Lou, M., Bing, L., Zhao, R., & Li, Z. (2015). Observation of oil spills through Landsat thermal infrared imagery: a case of Deepwater horizon. *Aquatic Procedia*, 3, 151–156.
- Zhao, J., Temimi, M., Ghedira, H., & Hu, C. (2014). Exploring the potential of optical remote sensing for oil spill detection in shallow coastal waters: a case study in the Arabian gulf. *Optics Express*, 22(11), 13755–13772.